Electronic Impurity Doping of a 2D Hybrid Lead Iodide Perovskite by Bi and Sn

Haipeng Lu,^{1,2,#} Gabrielle Koknat,^{3,#} Yi Yao,³ Ji Hao,¹ Xixi Qin,³ Chuanxiao Xiao,¹ Ruyi Song,⁴ Florian Merz,⁵ Markus Rampp,⁶ Sebastian Kokott,⁷ Christian Carbogno,⁷ Tianyang Li,³ Glenn Teeter,¹ Matthias Scheffler,⁷ Joseph J. Berry,^{1,8,9} David B. Mitzi,^{3,4} Jeffrey L. Blackburn,¹ Volker Blum*,^{3,4} and Matthew C. Beard*,^{1,8}

Corresponding Author

Volker Blum*: volker.blum@duke.edu

Matthew C. Beard*: <u>Matt.Beard@nrel.gov</u>

Contributed equally

ABSTRACT

Control over conductivity and carrier type (electrons/holes) defines semiconductors. A primary approach to target carrier concentrations involves introducing a small population of aliovalent impurity dopant atoms. In a combined synthetic and computational study, we assess impurity doping by introducing Bi and Sn in the prototype 2D Ruddlesden–Popper hybrid perovskite phenylethylammonium lead iodide (PEA₂PbI₄). Experimentally we demonstrate that Bi and Sn can achieve n- and p-type doping, respectively, but the doping efficiency is low. Simulations show that Bi introduces a deep defect energy level (~0.5 eV below the conduction band minimum) that contributes to the low doping efficiency, but to reproduce the low doping efficiency observed experimentally an acceptor level must also be present that limits n-type doping. Experiments found

¹ Material Chemical and Computational Science Directorate, National Renewable Energy Laboratory, Golden, Colorado 80401, United States

² Department of Chemistry, The Hong Kong University of Science and Technology, Clear Water Bay, Kowloon, Hong Kong, China (SAR)

³ Thomas Lord Department of Mechanical Engineering and Material Science, Duke University, Durham, North Carolina 27708, United States

⁴ Department of Chemistry, Duke University, Durham, North Carolina 27708, United States

⁵ Lenovo HPC Innovation Center, Meitnerstr. 9, D-70563 Stuttgart, Germany

⁶ Max Planck Computing and Data Facility, Giessenbachstrasse 2, D-85748 Garching, Germany

⁷ The NOMAD laboratory at the Fritz Haber Institute of the Max Planck Society, Faradayweg 4-6, D-14195 Berlin, Germany

⁸ Renewable and Sustainable Energy Institute, University of Colorado Boulder, Boulder, Colorado 80309, USA

⁹ Department of Physics, University of Colorado Boulder, Boulder, Colorado 80309, USA

that Sn achieves *p*-dopant behavior and simulations suggest this occurs through additional oxidation of Sn defects. We also studied how substitutional Bi incorporation can be controlled by tuning the electrochemical environment during synthesis. First-principles impurity doping simulations can be challenging: typical dopant concentrations constitute less than 0.01% of the atoms, necessitating large supercells, while a high level of theory is needed to capture the electronic levels. We demonstrate simulations of complex defect-containing unit cells that include up to 3,383 atoms, employing spin-orbit coupled hybrid density functional theory. While p- and n- type behavior can be achieved with Sn and Bi, simulations and experiments provide concrete directions where future efforts must be focused in order to achieve higher doping efficiency.

Popular Summary Combining experimental results with high fidelity band structure calculations, we demonstrate that 2D lead-halide perovskite semiconductors can be fabricated n or p-type when Bi³⁺ or Sn²⁺, respectively, replace Pb²⁺ in the lattice. Simulations show that reducing conditions during synthesis facilitate aliovalent n-type doping by Bi. Hybrid density functional theory simulations of complex defect-containing unit cells with up to 3,383 atoms properly capture the physicochemical behavior of isolated impurity dopants. The combination of (i) experimentally tracked Fermi levels as a function of impurity incorporation, (ii) a conceptual model of Fermi level evolution and (iii) hybrid DFT simulations enables us to shed light on the doping mechanism. We show that any n-type doping would be limited by a fairly large concentration of defects that trap the electrons donated by the n-type dopant incorporation, while p-type doping by Sn²⁺ is limited by Pb²⁺ vacancy formation.

Introduction

Two-dimensional (2D) hybrid organic-inorganic metal halide perovskites (MHPs) have recently emerged as promising semiconductors for solar cells, light-emitting diodes, opto-spintronics, and photodetectors. ¹⁻⁶ Their rich chemical and structural tunability provides unique opportunities to control for example their structural distortion, quantum and dielectric confinement, exciton—phonon coupling, and Rashba splitting, which, in turn, modulate their optical, electronic, thermal, and spin properties. High crystalline quality, even for low-temperature solution-phase synthesis, adds to their promise. However, one significant drawback relates to the ability to precisely control their Fermi level, charge carrier densities and majority carrier types. ⁷⁻⁸ In traditional inorganic semiconductors, efficient control of carrier type and density is generally achieved by introducing impurity aliovalent atoms, i.e., dopants. In organic semiconductors, the carrier concentration and conductivity can be similarly tuned over many orders of magnitude by employing molecular dopants. ⁹ MHPs possess both organic and inorganic sub-components and the variety of doping mechanisms are not fully understood, contributing to electronic doping that is much less efficient. ⁸, ¹⁰⁻¹¹

Past studies aiming to control doping in MHPs focused mostly on prototype 3D systems APbX₃ (X=Cl, Br, I; A =MA (methylammonium), FA (formamidinium), Cs). For example, aliovalent cations¹²⁻¹⁵ such as Bi³⁺ increased the conductivity of MAPbBr₃ single crystals by 4 orders of magnitude, with an increase of *n*-type carrier concentration (from $\sim 10^9$ cm⁻³ to $\sim 10^{11}$ – 10^{12} cm⁻³).¹² Bi³⁺-doped MAPbI₃ single crystals also display resistivity that is reduced by 3 orders of magnitude compared to undoped single crystal MAPbI₃ (from 10^8 Ω /cm to 10^5 Ω /cm).¹⁶

Interestingly, doping with isovalent ions (*e.g.* Mg²⁺, Sr²⁺, Sn²⁺)^{11, 17-18} can also tune the MAPbI₃ Fermi level, with doping mechanisms that vary under different doping regimes (concentration). Computationally, substituting Bi for Pb was shown to form relatively deep defect levels in 3D MHPs including CsPbBr₃, CsPbCl₃, MAPbBr₃ and MAPbI₃, for which predicted (+/0) transition levels range from 0.26 eV to 0.59 eV below the conduction band minimum (CBM). Report However, predictions for FAPbI₃¹⁹ and CsPbI₃²⁰ indicate a much shallower dopant character, with (+/0) transition levels at 0.05 eV and 0.1 eV, respectively. In contrast, electronic doping in the 2D counterparts is understudied, although several reports have shown that impurity atoms (*e.g.* Bi³⁺, Mn²⁺, Sn²⁺)²⁶⁻³¹ can be introduced into 2D MHPs to elicit interesting optical properties. For instance, Li *et al*³¹ showed that a small amount of isovalent Sn²⁺ dopants induces a broadband emission in phenylethylammonium lead iodide PEA₂PbI₄ crystals, resulting from self-trapped excitons. Lyu *et al*.²⁶ demonstrated that Bi³⁺-doped 2D BA₂PbI₄ crystals exhibit a new near-infrared (NIR) emission. However, electronic doping, i.e., modulation of carrier type, density, and Fermi level, has not been demonstrated in lead-based 2D MHPs.

In the present work, we experimentally and computationally study electronic doping of the prototype 2D Ruddlesden–Popper PEA₂PbI₄ via both aliovalent Bi³⁺ (n-type doping) and isovalent Sn²⁺ cations (*p*-type doping). Another doping strategy, not studied here, is to use molecular donors or acceptors intercalated into the organic layer³² similar to studies at surfaces of 3D MAPbI₃.³³⁻³⁴ The choice of PEA₂PbI₄ as a target is motivated by the fact that this system is, to our knowledge, the first 2D organic-inorganic MHP synthesized with a conjugated group (phenyl ring)³⁵, is widely studied, and the ability to successfully dope PEA₂PbI₄ would likely translate to the much broader class of other 2D MHPs. In our study, we find that both Bi³⁺ and Sn²⁺ can be substitutionally incorporated into PEA₂PbI₄ crystals, with drastically different incorporation efficiencies. Small amounts of incorporated Sn²⁺ or Bi³⁺ directly modulate the electronic structure, studied here with first-principles, spin-orbit coupled hybrid density functional theory (DFT). This level of theory is computationally demanding but necessary to capture electronic band edge trends.³⁶ Importantly, our work overcomes a frequent drawback of such first-principles calculations for large, complex semiconductor structures, namely that calculations are typically limited to supercell models with a few hundreds of atoms including all organic and inorganic components. Even when substituting just a single Pb²⁺ ion with an impurity in these limited supercells, the results are still closer to alloving (high impurity concentration) rather than to the dilute limit of impurity doping (low concentrations). Accordingly, the electronic levels induced by point defects in neighboring supercells of insufficient size can interact and may not capture the physicochemical properties of dilute impurity doping. Here, we demonstrate a computational enhancement of a high-precision, all-electron hybrid DFT implementation in the electronic structure code FHI-aims, ³⁷⁻⁴¹ allowing investigation of supercells with up to 3,383 atoms to accurately capture the impurity limit in energy band structures. Our approach includes spin-orbit coupling⁴¹ (SOC) and uses a single, consistent density functional for both valence and core states, avoiding potential errors introduced by corevalence inconsistencies⁴² (note that the static exchange term is the largest contribution to the corevalence error in Ref. 42).

A key demonstration of the current study is the synergistic understanding of MHP doping that emerges from our simulations when coupled with targeted experiments. The simulations provide direct access to the energy of the defect level, a quantity that is not unambiguously accessible in experiment. Complementary experimental assessments, including conductivity measurements and X-ray photoelectron spectroscopy (XPS) as a function of input impurity concentration, reveal the Fermi level modulation as a function of dopant incorporation. In combination, our results demonstrate electronic doping by Bi³⁺ and Sn²⁺ in PEA₂PbI₄, and provide crucial insight into the underlying mechanisms. For isovalent Sn_{Pb} substitutions, our calculations support indirect doping by promoting Pb²⁺ vacancy formation in close proximity and forming a shallow acceptor level as one possible mechanism. For Bipb substitutions, but likely also affecting other n-doping mechanisms, we identified a population of acceptors that currently limits n-type doping efficiency in PEA₂PbI₄. To achieve a larger control over the Fermi level our results suggest that not only does Bi, perhaps the single most intuitive candidate *n*-dopant for a Pb-based semiconductor system, have too deep of a defect level but also that the doping efficiency is significantly hindered by these compensating acceptors. We find that the acceptors are independent of the Bi chemistry and therefore conclude that doping would be hindered even with a dopant that has a shallower defect level, i.e., they would hinder any attempt at n-type doping. While we do not uncover here the chemical identity of the compensating defect, we can place limits on its characteristics and provide avenues towards understanding defects in future and ongoing work.

Results and Discussion

Doping in PEA₂PbI₄ crystals. Single crystals of undoped, Bi³⁺-doped, and Sn²⁺-doped 2D PEA₂PbI₄ (**Figure 1A**) were synthesized from a concentrated hydroiodic acid (HI) solution, containing hypophosphorous acid (H₃PO₂) as a reducing agent. (See Methods). Small dopant equivalents were introduced by adding Bi₂O₃ or SnO₂ with different nominal ratios of Bi:Pb or Sn:Pb into the reaction mixture, while keeping the total metal content constant. Sn⁴⁺ is reduced to Sn²⁺ *in-situ* by hypophosphorous acid; Bi³⁺ may also be reduced to Bi²⁺ (formally) when substitutionally incorporated for Pb²⁺, facilitating *n*-type doping. In the following, we follow the convention of denoting doped samples as x% Bi or x% Sn, where x% corresponds to the atomic *input* ratio of Bi³⁺ or Sn²⁺ relative to Pb²⁺ in the feed solutions and not the incorporated impurity content.

The incorporation efficiency is studied by Inductively Coupled Plasma Mass Spectrometry (ICP-MS) (**Figure 1B**) and is 0.013 ± 0.002 and 1.03 ± 0.02 for Bi³⁺ and Sn²⁺, respectively, (errors are from best fit of a line to the data in Fig. 1B) indicating a 100 times higher incorporation efficiency of Sn²⁺ compared to Bi³⁺, consistent with the low inter-exchange energy of Pb²⁺ and Sn²⁺. A incorporation efficiency greater than 1 could be associated with a concomitant increase in Pb vacancies. As the dopant concentration increases, the color of Bi³⁺-doped PEA₂PbI₄ crystals gradually changes from orange to dark red and eventually to black (inset, Fig. 1C), while that of Sn²⁺-doped PEA₂PbI₄ crystals changes from orange to deep red (inset, Fig. 1C), suggesting a significant effect on the electronic structure.

Linear optical properties of powders were measured by diffuse reflectance spectroscopy, and absorption spectra were obtained using the Kubelka-Munk equation: $\alpha/S = (1 - R)^2/(2R)$, where α is the absorption coefficient, S is the scattering coefficient, and R is the absolute reflectance (**Figure 1C**). Despite the striking color change clearly observed upon Bi³⁺ or Sn²⁺ incorporation. the absorption spectra of doped PEA₂PbI₄ mostly reproduce that of undoped PEA₂PbI₄ with an exciton peak at 514 nm. When normalized at the higher energy bands (300 – 450 nm) we find that the exciton peak absorption is slightly quenched, suggesting the presence of excess delocalized electrons/holes that partially block exciton transitions. This excitonic quenching results from the phase-space filling effect, which has been discussed extensively for other excitonic semiconductors. 46-48 An additional absorption tail at longer wavelengths apparently accounts for the color change. In contrast to Bi3+, even of 1% input Sn changes the absorption spectra significantly, confirming a higher incorporation efficiency for Sn²⁺ compared to Bi³⁺. It is worth noting that the absorption tails associated with Bi³⁺ vs. Sn²⁺ may arise for different underlying reasons. We tentatively associate the tail for Bi³⁺, which has low incorporation efficiency, with the defect states that it introduces (see below). In contrast, Sn²⁺ has a much higher incorporation efficiency and the overall reduction of the band gap by Sn²⁺ incorporation may be responsible for the tail. A similar tail appears, e.g., in the layered perovskite (R-MBA)₂Pb_{1-x}Sn_xI₄ (R-MBA=Rmethylbenzylammonium) at Sn input levels x=0.05 and was tentatively attributed to areas of locally higher Sn²⁺ concentration and associated lower band gaps due to inhomogeneous Sn distribution.44

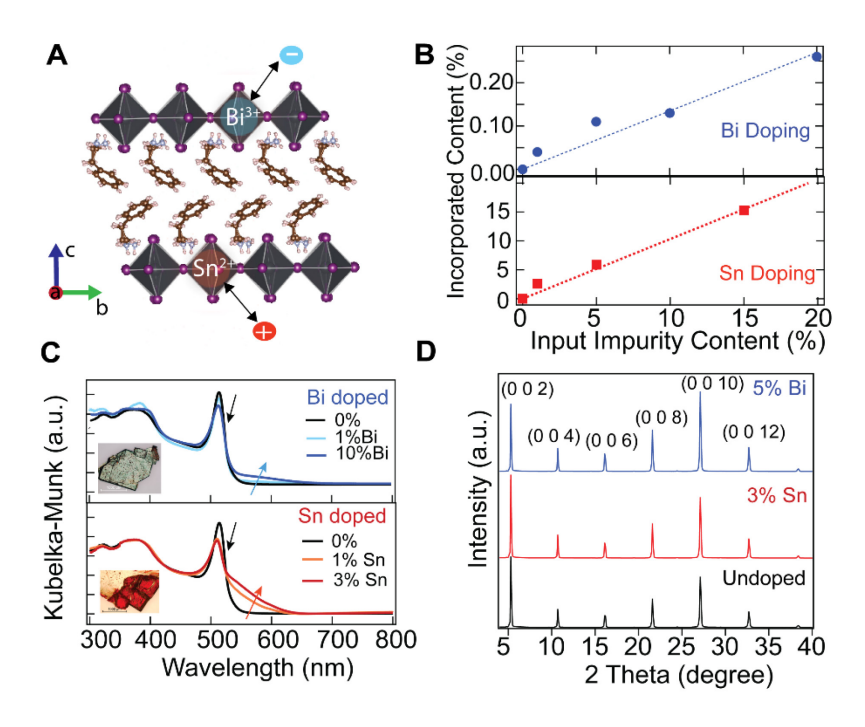


Figure 1. (A) Crystal structure of PEA₂PbI₄ and the illustrative doping effects by impurity atoms. (B) Summary of ICP-MS data showing the ratio of incorporated dopants relative to Pb to input dopants for Bi and Sn, respectively. The dotted lines indicate estimated linear approximations to the dopant incorporation levels as a guide to the eye. (C) UV-vis absorption spectra of undoped, Bi³⁺-doped and Sn²⁺-doped

PEA₂PbI₄. x% corresponds to the input atomic ratio of Bi³⁺ or Sn²⁺ relative to Pb²⁺, inset shows optical images of the as-grown doped crystals. (D) PXRD spectra of undoped, 5%Bi³⁺-doped and 3%Sn²⁺-doped PEA₂PbI₄ crystals.

Powder X-ray diffraction (PXRD) pattern of undoped, 5% Bi³⁺-doped and 3% Sn²⁺-doped PEA₂PbI₄ crystals all show the same patterns (*i.e.* (002*l*) peaks, **Figure 1D**), indicating no significant impact on the crystal structure when incorporating dopant atoms. The observed peaks represent the interlayer distance between inorganic Pb-I sheets, which is mostly defined by the organic cations and remains unchanged. While the space group of the undoped PEA₂PbI₄ crystals was refined to centrosymmetric *P*-1, we found that the 3% Bi³⁺-doped crystals could be refined to either centrosymmetric *P*-1 or noncentrosymmetric *Cc* space groups (Supporting Information (SI), Table S4.1). This effect is similar to previous single-crystal XRD (SC-XRD) on Sn²⁺-doped crystals that found a change of the space group, ³¹ suggesting successful Bi³⁺ incorporation.

Computational Approach: Doping effects of Sn²⁺ and Bi³⁺ in PEA₂PbI₄ crystals. We performed first principles calculations based on spin-orbit coupled hybrid DFT⁴¹. The screenedexchange HSE06 density functional⁴¹⁻⁴² was used with standard parameters (exchange mixing 0.25, screening parameter 0.11 (Bohr radii)⁻¹).⁴⁹ The present choice qualitatively captures energy band alignments in Pb-based layered MHPs and quantitatively underestimates their band gaps by a few tenths of eV. 50-52 This underestimation falls into the general range of prediction errors of this parameterization of the HSE06 density functional for semiconductors in this band gap range.⁵³ Thus, the HSE06 parametrization used here is expected to be appropriate for the present Pb- and Bi- containing metal-halide perovskites. We optimized the existing implementation³⁹ of hybrid DFT in the high-precision, all-electron electronic structure code FHI-aims³⁷⁻⁴¹, allowing up to 3,383 atom supercells to be modeled. Fully relaxed atomic structures (lattice parameters and atomic positions) obtained at the level of dispersion-corrected semilocal DFT (PBE functional⁵⁴ including the Tkatchenko-Scheffler (TS) correction⁵⁵) were used for the underlying geometries. This level of theory has yielded atomic structures in close agreement with experimental structures for other organic-inorganic hybrids (see Table S4.2 for a comparison of experimental and computational lattice parameters of different organic-inorganic hybrids at this level of theory; deviations are typically well below 2%). 6, 44, 50-51 For the calculation of defect energy levels, we use generalized Kohn-Sham eigenvalue differences derived from the HSE06+SOC functional, based on the observation that this non-local density functional comes close to satisfying the generalized Koopman's theorem (gKT) as outlined in more detail in Ref. ⁵⁶. With this approach, we are able to avoid the introduction of supercell calculations with an explicit artificial background charge and associated charge corrections⁵⁷⁻⁵⁹ that would be required when employing total-energy differences of charged supercells. The calculated supercells in this work are all electrically neutral. The applicability of the gKT essentially relies on the fact that differences between occupied defect levels and unoccupied band edges take on the role of the fundamental gap in a defect-free systems. For predictions of the fundamental gap, the qualitative accuracy of the HSE06+SOC functional for the prediction of band gaps of semiconductors has been established in numerous references over the years. ^{49, 51, 53, 60} We note that including SOC is critical since it can shift energy bands associated

with the Pb/Bi 6p electron derived conduction bands by ~1eV relative to one another (see references 41, 50, 51 and Figure S2.15) The qualitive agreement of our computational predictions with energy levels derived from a model of the observed Fermi level shift with Bi incorporated concentration in PEA₂PbI₄, which also reveals the likely presence of a set of deeper-lying intrinsic defect states (see below), further validates our approach.

Incorporation mechanisms of Sn²⁺

According to previous observations,³¹ isovalent Sn²⁺ undergoes substitutional doping, replacing Pb²⁺. A 1,504-atom structure with a substitution of one in 32 Pb atoms by Sn, shown in Figure 2A and B and referred to as (4×4)-Snpb, was simulated (Figure 2C). This supercell models a substitution of 3% of Pb atoms by Sn. In interpreting this value, it is important to note that the overall number of atoms in the supercell is much larger than just the number of Pb sites. The Sn incorporation corresponds to a substitution of less than 0.07% of atoms overall. In this limit, Sn incorporation slightly reduces the bandgap to 1.95 eV, compared to 2.01 eV in the pristine structure, consistent with previous observations.⁶¹⁻⁶³ With increasing Sn content (Figures S1.9–S1.11), the band gap narrows further (Figures S2.9-S2.11, S3.8-S3.10). A largely halide-derived state with contributions from Sn^{2+} s states forms at the top of the valence band. However, already in the limit of Figure 2C, the associated band is not energetically separated from Pb-I states (given the only ~60 meV difference between the 1.95 eV band gap and the pristine case). A visualization of this topmost Sn-derived valence orbital at the Γ point (yellow isosurface in Figure 2A) indicates significant delocalization, consistent with hybridization with Pb²⁺ states. Overall, this scenario is closer to the formation of an alloy than to that of a traditional dopant state, even for the large (4×4) defect arrangement. Sn²⁺ does not itself provide an acceptor state; however, it is known that oxidation of the Sn-derived state can introduce holes. 17-18 This oxidation-assisted p-doping is the likely active mechanism in the experimental samples reported here as well.

We validated the hypothesis of oxidation-driven p-doping from Sn by direct calculations shown in **Figures 2E-H (and Fig. S1.12-S1.15, S2.12-S2.14),** using a nearby Pb²⁺ vacancy as a plausible oxidizing agent. Specifically, the placement of the Pb²⁺ vacancy directly next to a Sn²⁺ dopant results in a shallow unoccupied level just above the valence band maximum (VBM) that is nevertheless separated (by a few meV) from the remaining states (**Figure 2G**). Formally, this state may be understood as the oxidation of Sn^{II} to Sn^{IV} in order to provide two otherwise missing electrons to the I^- anions adjacent to the Pb²⁺ vacancy. Indeed, the isosurface density plot (**Figure 2E**) shows that this state is largely localized at the I^- anions near the Sn_{Pb} substitution and the adjacent Pb²⁺ vacancy. The now-empty level is the Sn-enriched level that is the highest occupied level in the vacancy-free structure, as shown by Mulliken population analyses of these states in **Figures 2D** and **2H**, respectively. For comparison, **Figures S1.15** and **Figures S2.14** show a structure model and band structures for a supercell with a Pb²⁺ vacancy and a Sn_{Pb} substitution placed in different inorganic layers, i.e., far away from one another. In this case, the empty state associated with the I^- anions near the Pb²⁺ vacancy is not energetically separated from the remaining valence states. Also, the DFT-PBE+TS total energy indicates that the formation of the

 Pb^{2+} vacancy is energetically favorable by ~0.3 eV if the vacancy is located next to the Sn_{Pb} defect, rather than far away from it. This energy difference provides a possible driving force for a p-type doping enhancement in the presence of Sn.

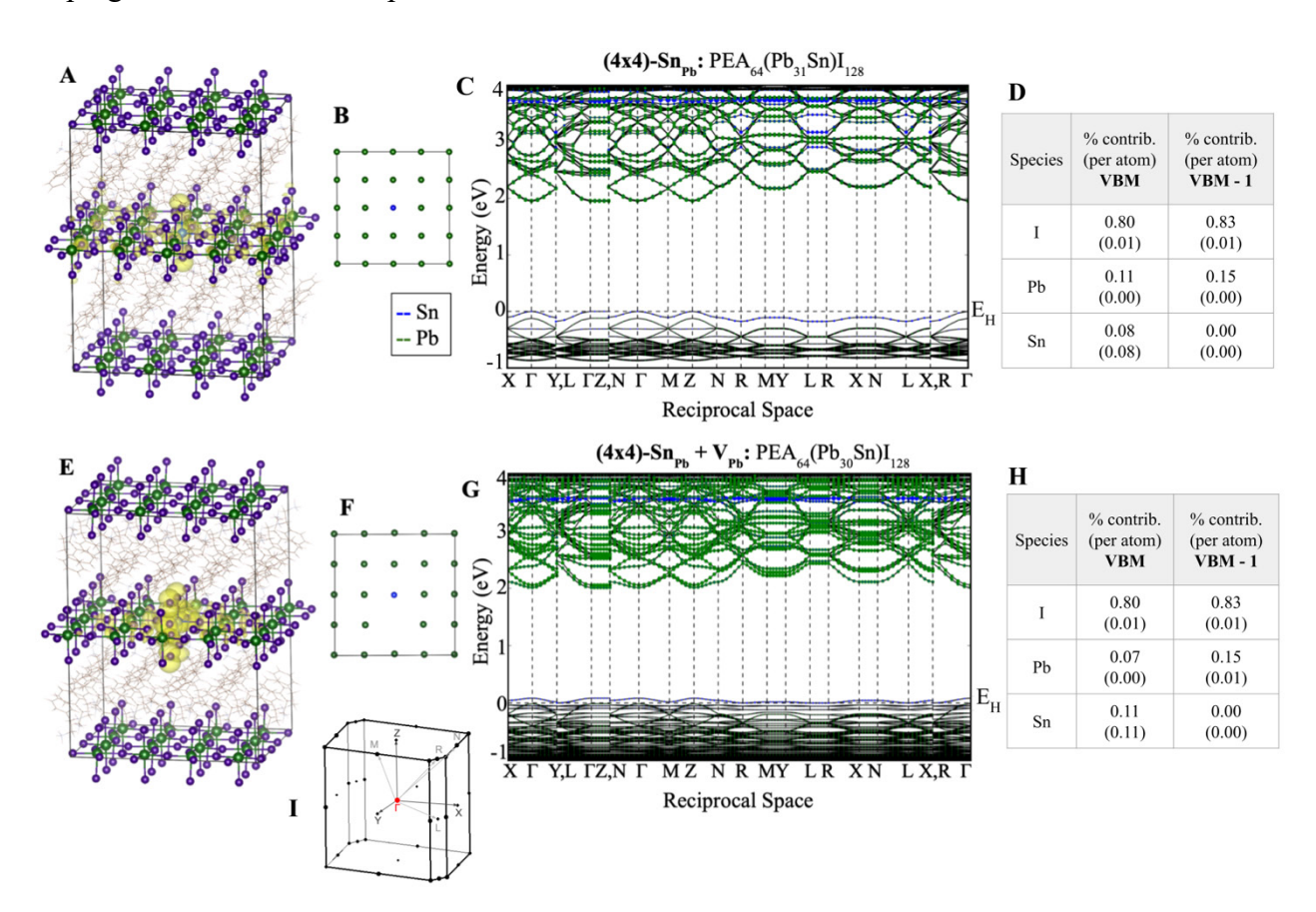


Figure 2. (4×4)-Sn_{Pb} and (4×4)-Sn_{Pb}+V_{Pb} structural models. (A) Full geometry of (4×4)-Sn_{Pb}: Pb in green, Sn in blue (atom in center), I in purple, wire models indicate PEA molecules. The orbital associated with the highest occupied Sn_{Pb}-derived state at the Γ point is shown by the yellow isosurface (of isosurface level 0.03 corresponding to |Ψ|), showing that this is an extended state, essentially hybridized with the host (PEA₂PbI₄) valence band. (B) Defect-containing layer of (4×4)-Sn_{Pb}, showing only the B-site atoms (Pb or Sn) for clarity. (C) Computed DFT-HSE06+SOC electronic band structure of (4×4)-Sn_{Pb}, Brillouin zone definition shown in (I). Contribution of B-site atoms to different bands, Pb is green and Sn is blue. Species contributions of Sn (blue) are layered on top of contributions from Pb (green). Note that the majority B-site contribution to the top of the valence band originates from Sn. The dashed black horizontal line labeled E_H indicates the energy above which states are unoccupied in the computation. (Note that this is not a Fermi level since the calculations do not include a formal temperature.) (D) Tabulated percentages of species contributions to the valence band maximum (VBM) and the electronic state with directly below the VBM (VBM-1) at the Γ point. Values are listed as total percentage, and percent per atom. Notice the high Sn-contribution (per atom) to the VBM. Analogous sub-figures (E-H) are given for the (4×4)-Sn_{Pb}+V_{Pb} structure.

Incorporation mechanism for Bi³⁺.

The incorporation of aliovalent Bi³⁺ could be accompanied by the formation of a compensating Pb²⁺ vacancy. We consider two plausible mechanisms. The first is substitutional doping, namely,

every Bi^{3+} ion directly substitutes a Pb^{2+} ion, requiring an extra electron to formally reduce Bi^{3+} to Bi^{2+} in order to balance the charge in the crystal, referred to as the reduced mechanism (1). When the extra electron associated with Bi^{2+} is ionized, n-type electronic doping results. In the unreduced mechanism (2), 2 Bi^{3+} ions substitute for 3 Pb^{2+} ions, generating a compensating B-site vacancy to balance the charge. Here, no weakly bound electrons or holes would be generated, and thus no electronic doping would result.

Reduced mechanism:

$$PEA_2PbI_4 + x Bi^{3+} + x e^{-} \rightarrow PEA_2(Pb_{1-x}Bi_x)I_4 + x Pb^{2+}$$
. (1)

Unreduced mechanism:

$$PEA_2PbI_4 + 2x/3 Bi^{3+} \rightarrow PEA_2(Pb_{1-x}Bi_{2x/3} \square_{x/3})I_4 + x Pb^{2+}$$
. (2)

Here, x denotes a fractional number quantifying Bi incorporation and \square denotes a structural vacancy at the Pb²⁺ site.

Schematic models of corresponding Bi dopant incorporation models in (4×4) arrangements with respect to the underlying B-site atom positions (either Pb or Bi) are shown in **Figure 3B**. Reduction-type doping, (1), was modeled through a 1,504-atom model, (4×4) -Bi_{Pb}, in which one Pb²⁺ (out of thirty-two) was replaced by one Bi³⁺ (reduced to Bi²⁺, in a spin-polarized calculation to account for the unpaired e⁻ situated at the Bi site). Again, in terms of the full structure, this model corresponds to substituting less than 0.07% of atoms overall. Non-reduction type doping, (2), was simulated through a 1,503-atom model, (4×4) -Bi₂ \Box , in which three Pb²⁺ were replaced by 2 Bi³⁺ and a vacancy. In the (4×4) -Bi₂ \Box model, the vacancy is placed near both Bi substituents, to satisfy local charge balance. Both modes of Bi³⁺ incorporation introduce defect states that are close to, but well separated from the conduction band edge (**Figures 3C,D**), reducing the electronic bandgap and thus offering a possible explanation for the experimentally observed low-energy tail of the UV-vis absorption spectrum.

The undoped PEA₂PbI₄ bandgap value is 2.01 eV (**Figures S1.1, S1.2, S2.1, S2.2, S3.1, S3.2**), while the highest occupied defect state in the substitutionally-doped (4×4)-Bi_{Pb} structure is approximately 1.47 eV above the VBM. Thus, the position of the Bi_{Pb}-induced defect states is ~0.5 eV below the CBM, consistent with computational predictions of similarly Bi-derived defect states in 3D metal-halide perovskites. ¹⁸⁻²⁴ The defect states in (4×4)-Bi₂ \square are unoccupied and situated somewhat higher, around 1.76 eV above the VBM, i.e., ~0.35 eV below the CBM. **Figures 3E,F** visualize the DFT-HSE06+SOC orbitals associated with Bi dopants in (4×4)-Bi_{Pb} and (4×4)-Bi₂ \square arrangements in PEA₂PbI₄. In line with the essentially flat defect band, the defect state associated with substitutional Bi²⁺ is localized within the (4×4) arrangement, indicating an electron bound to Bi³⁺ at T=0. Likewise, the defect state associated with the Bi₂ \square defect is well localized; however,

it does not contain electrons but could act as an acceptor for any free electrons, i.e. its formation would be detrimental to *n*-type doping.

These trends are not apparent from smaller models comprising 188, 376, and 751 atoms, respectively, each featuring a single Bi_{Pb} or Bi₂ defect (see Figures S1.3-S1.7, S2.3-S2.7, and **S3.3-3.7**). Smaller structure models result in larger overlap between orbitals of the neighboring atoms, which results in larger dispersion of the energetic states, as illustrated in the band structure figures. This overlap obfuscates electron location, therefore making conclusions about occupation more elusive. Importantly, in Figures 3C,D, the electronic levels associated with Bi defects in adjacent supercells appear to be essentially decoupled from one another (indicated by the largely flat bands). While the ratio of Bi impurities to Pb sites in the model (3%) is still a factor of 30 higher than the incorporated impurity content seen in Figure 1B, the electronic characteristics of an isolated Bi_{Pb} defect are captured by the 1,504-atom supercell and would no longer change substantially even if the supercell size were increased further. For the Bi₂ defect, Figure 3D still shows some residual dispersion in the empty states associated with Bi³⁺, consistent with the fact that the two Bi sites are only separated by one Pb site (and associated halide anions) as seen in Figure 3F. However, the Bi₂ \square derived states in a smaller, 751-atom (2×4) model (Figures S1.5 and S2.5) are much more dispersive than their counterparts in the (4×4) model (Figure 3D), showing that it essentially approaches the dilute limit of the Bi₂ defect. In order to unambiguously clarify the nature of the empty Bi₂□ defect bands as localized flat bands that are well separated from the PEA₂PbI₄ conduction bands, we additionally include a band structure calculation of a 3,383-atom, (6×6) arrangement of Bi₂□ defects (Figure S2.8) using DFT-HSE06+SOC and FHI-aims' intermediate settings. As expected, the Bi-derived states become essentially completely flat and retain their character as unoccupied defect states that are close to but clearly separated from, the PEA₂PbI₄ host conduction bands. The unusually demanding computational cells of >3,000 atoms used here allow us to unambiguously demonstrate the nature of the Bi²⁺ derived orbitals as localized dopant-like states that are cleanly separated from the energy bands associated with the PEA₂PbI₄ host system.

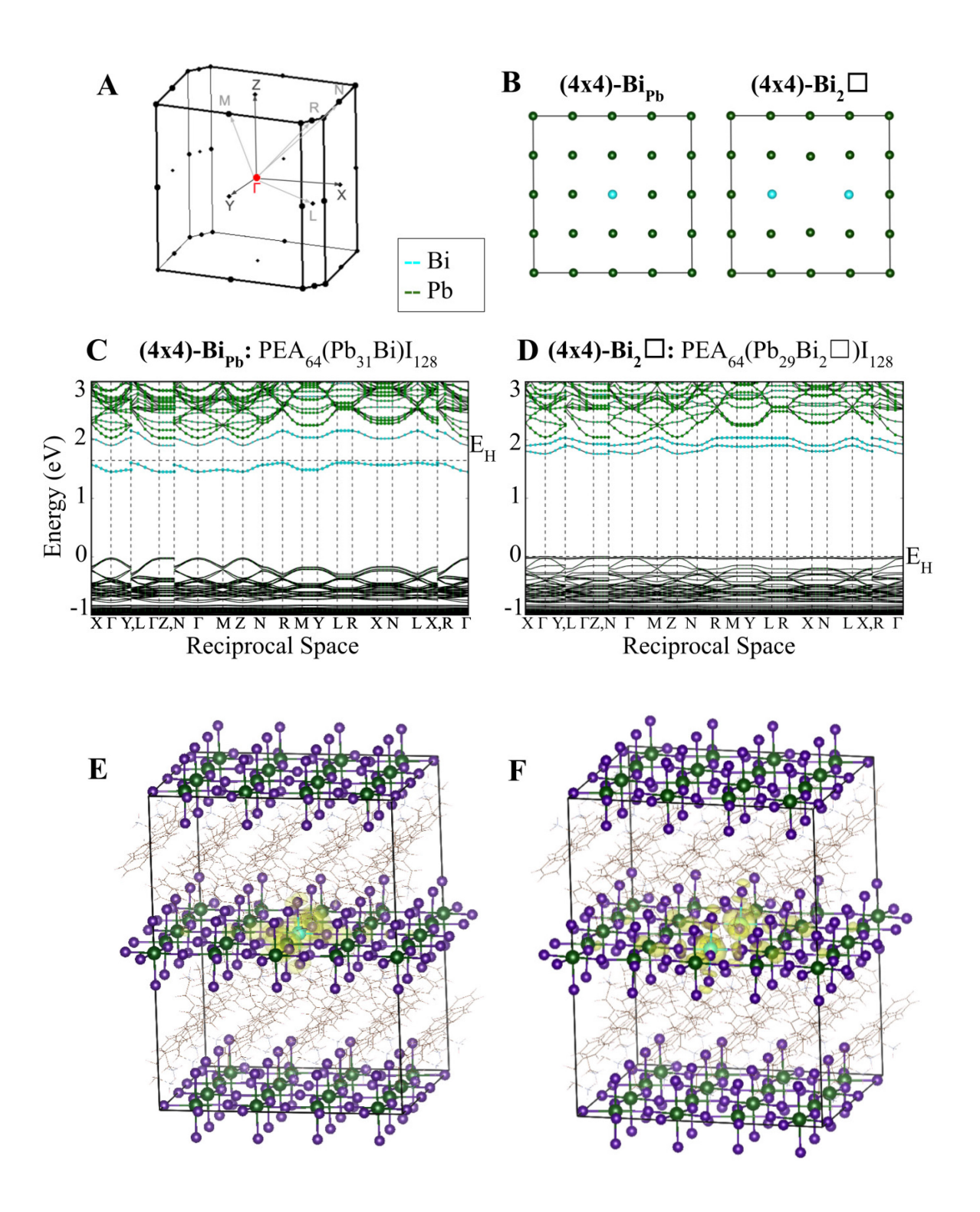


Figure 3. Structure models, DFT-HSE06+SOC predicted band structures and orbitals for the reduced and non-reduced Bi-incorporated structures (4×4)-Bi_{Pb} and (4×4)-Bi₂ \square , respectively (see text). (A) Brillouin zone. (B) Impurity-containing layers of the substitutional defect and the vacancy forming defect models, showing B-site positions - Pb (green), Bi (cyan), or vacancy - only for clarity. (C) and (D): Computed DFT-HSE06+SOC electronic band structures of (C) substitutionally-doped (4×4)-Bi_{Pb} (spin-polarized) and (D) vacancy structure (4x4)-Bi₂ \square . Bands highlighted in green are predominantly derived from Pb, bands highlighted in cyan are predominantly derived from Bi. The highest occupied level in (C) is the band around 1.5 eV. (E) Orbital associated with the occupied Bi-derived defect band at the Γ-point of (4×4)-Bi_{Pb}, shown for an isosurface value (corresponding to |Ψ|) of 0.03. (F) Analogous to (E), but for (4x4)-Bi₂ \square . Atom/molecule identification: Pb (green), Bi (cyan), I (purple), wireframe (PEA). The dashed black horizontal lines labeled E_H in (E) and (F) indicate the energy above which states are unoccupied in the computation. (Note that this is not a Fermi level since the calculations do not include a formal temperature.)

Chemical nature of impurity doping. To estimate whether (1) or (2) is more favorable, we compared DFT derived formation energies of substitutional vs. vacancy-forming defects. As written, equations (1) and (2) are incomplete since they lack anions and/or electron sources that are determined by the synthetic environment. In our specific case, we can substitute with specific compounds present during synthesis as follows:

This substitution changes Eq. (1) to:

$$PEA2PbI4 + x/2 Bi2O3 + x/2 H3PO2 \rightarrow PEA2(Pb1-xBix)I4 + xPbO + x/2 H3PO3$$

$$\downarrow +xe^{-}$$

This substitution changes Eq. (2) to:

$$PEA_2PbI_4 + x/3 Bi_2O_3 \rightarrow PEA_2(Pb_{1-x})Bi_{2x/3} \square_{x/3} I_4 + x PbO.$$
 (4)

The key difference is that reaction pathways (1)/(3) require an electron source, whereas (2)/(4) do not depend on the chemical potential of electrons, i.e., on reducing vs. oxidizing conditions. In Eq. (3) we explicitly show that electrons must transfer to Bi³⁺ from H₃PO₂ forming Bi²⁺ and H₃PO₃, while in Eq. 4 the formal oxidation state of Bi remains the same. To illustrate the impact of the range of possible experimental conditions, we consider two alternative electron-providing half-reactions, that while not expected under our synthetic environment, could hypothetically serve as electron sources:

$$O^{2-} + H_2 \rightarrow H_2O + 2e^-,$$
 (5)

$$O^{2-} \rightarrow 1/2 O_2 + 2e^{-}$$
 (6)

In **Table 1**, we summarize defect formation energies at the level of DFT-PBE+TS, for reaction pathways (3), (1)+(5), (1)+(6) and (4). We compare energies for different supercell models, up to the largest, (4×4) defect models. Pathway (4) does not depend on the presence or absence of a reducing agent and leads to a high positive formation energy of \sim 2 eV. In contrast, the formation

energy for the reducing mechanism depends on the electron source: For H_3PO_2 or H_2 , a defect formation energy (per Bi atom) of ~0.7–0.8 eV results, while, assuming O_2 formation from O^{2-} as the only available reservoir leads to less favorable conditions (2.4 eV).

Table 1. Computed defect formation energies of different Bi-incorporation mechanisms, i.e., for H_2 , O_2 , and H_3PO_2 considered as electron sources. The defect energies are given per defect, i.e. per single Bi_{Pb} substitution and per single $Bi_2\Box$ composite defect. See the SI *Section I: Structure details for DFT calculations* for an overview of the models employed and **Table S10.1** for the exact reaction equations used for each defect model. Values given for (4×4) -Bi_{Pb} are calculated for the spin-polarized system, where the spin polarization energy was calculated using intermediate settings in FHI-aims. See **Tables S10.1** and **S10.3** for reaction equations and total energy values.

$\Delta E_{ m defect}$	Electron source	(c2×2)-Bi _{Pb} : PEA ₈ (Pb ₃ Bi)I ₁₆	(2×2)-Bi _{Pb} : PEA ₁₆ (Pb ₇ Bi)I ₃₂	(2×4)-Bi ₂ \square : PEA ₃₂ (Pb ₁₃ Bi ₂ \square)I ₆₄	(4×4)-Bi _{Pb} : PEA ₆₄ (Pb ₃₁ Bi)I ₁₂₈	(4×4) -Bi ₂ \square : PEA ₆₄ $(Pb_{29}Bi_2\square)I_{128}$
Formation Energy (eV)	H_2	0.682	0.618	2.076	0.762	1.957
	O_2	2.296	2.231		2.375	
	H ₃ PO ₂	0.626	0.561		0.705	

The results (**Table 1**) are qualitative in nature, they assume specific reagents, rely on gas-phase computed total energies, and do not account for concentrations and/or partial pressures. Nevertheless, the calculated defect incorporation energies illustrate our key point, which is that the environment employed when incorporating electronic dopants during synthesis can determine whether a reduced form (no compensating vacancies) or oxidized form (with compensating vacancies) of a particular dopant is incorporated. Our synthesis included a reducing agent, H₃PO₂, thus we expect that Bi is predominantly incorporated as a substitutional dopant without forming compensating vacancies. In contrast to Bi, the formation energies computed for Sn incorporation and using our experimental reagents are always favorable (see **Tables S10.2 and S610.4**, consistent with the experimental conclusion that essentially all available Sn is incorporated into the synthesized crystals. The calculated formation energies per incorporated Sn atom for different Sn-impurity structures are as follows: 3%-impurity structure, (4×4)-Sn_{Pb}, -0.233 eV/Sn; 50% alloyed, c(2×2)-Sn_{Pb}, -0.233 eV/Sn; fully substituted structure, (c2×2)-Sn_{Pb}, -0.240 eV. The calculated energy values per Sn atom do not vary appreciably with Sn concentration, consistent with the idea that a substitutional alloy without strong Sn-Sn attraction or repulsion forms.

Impurity doping in PEA₂PbI₄ thin films. When single crystals of undoped, Bi³⁺-doped, and Sn²⁺-doped PEA₂PbI₄ were dissolved in DMF and spin-cast onto quartz substrates, they did not display changes of their crystal structure or any changes in preferred film orientation of the doped vs. undoped films(XRD, **Figure S5.1**). UV-vis exhibited similar behavior as the powder samples, i.e.,

quenched exciton absorption, an absorption tail (**Figure S6.1a**), and the films exhibited quenched photoluminescence (PL) (**Figure S6.1b**) with the degree of PL-quenching strongly related to the incorporated dopant concentration, i.e., more dopants result in larger PL quenching. Time-resolved photoluminescence (TRPL) measurements indicate the PL lifetime (~ 1.1 ns mono-exponential decay) remains essentially the same for Bi- and Sn- incorporation, likely due to low incorporated metal concentration (**Figure S6.1c**). High resolution X-ray photoelectron spectra (HR-XPS) show the presence of both Sn²⁺ and Sn⁴⁺ in 3%Sn-doped films (**Figure S7.1**) consistent with partial oxidation of Sn²⁺ to Sn⁴⁺, while the Bi incorporated content was too low to detect by XPS. Scanning electron microscopy (SEM) images showed very similar morphology and roughness for the undoped and doped films and energy-dispersive X-ray spectroscopy (EDX) revealed a homogeneous distribution of Sn and Bi (submicron resolution) with no obvious dopant segregation (**Figure S8.1**). Thus, evidence that the Sn/Bi impurities incorporated into crystals is also incorporated into the films is from the optoelectrical measurements, we assume that the amount incorporated in the films is proportional to that in the crystals.

Electronic doping in PEA₂PbI₄ thin films. All PEA₂PbI₄ thin films were measured with air-free methods to eliminate any impacts of external oxidation during their characterization. Four-point probe sheet resistance measurements were obtained by averaging values from 5 different random spots, with resistivities in the $10^{10} \Omega/\text{sq}$ range. As the Sn or Bi dopant concentration increased, the sheet resistance decreased then gradually plateaued (Figure 4A). 3%Sn-doped and 20%Bi-doped PEA₂PbI₄ thin films display a 30% and 50% reduction in sheet resistance, respectively, suggesting an increased population of delocalized electrons/holes. Concurrently, HR-XPS of the valence band edge region (Figure 4B-C) exhibited a shift of valence band maximum (E_{VBM}) with respect to the Fermi level $(E_{\rm F})$ upon doping (note that in the XPS data the Fermi level is the reference energy and is set to zero). While we appreciate that the XPS probes mostly the surface region of the films, we assume that the bulk Fermi level tracks that of the surface Fermi-level. The $E_F - E_{VBM}$ for the undoped PEA₂PbI₄ film is 1.49 eV. Assuming the bandgap (E_g) equals the sum of exciton energy (514 nm or 2.41 eV) and the exciton binding energy (0.26 eV), 64 i.e. $E_g = 2.41 + 0.26 = 2.67 \text{ eV}^{52}$, the undoped PEA₂PbI₄ is slightly n-type. Bi³⁺ dopants shift E_{VBM} further from E_F , indicating more n-type behavior, with a shift as large as 440 meV that levels off at higher Bi input, similar to the trend in resistance. On the other hand, when Sn^{2+} is added, the E_{VBM} shifts closer to E_{F} , indicating a more p-type film. The Fermi level shift is as large as ~200 meV in 3%Sn-doped PEA₂PbI₄. The resistance measurements and XPS data demonstrate that incorporated Bi³⁺ dopants introduce delocalized electrons while Sn²⁺ dopants induce delocalized holes.

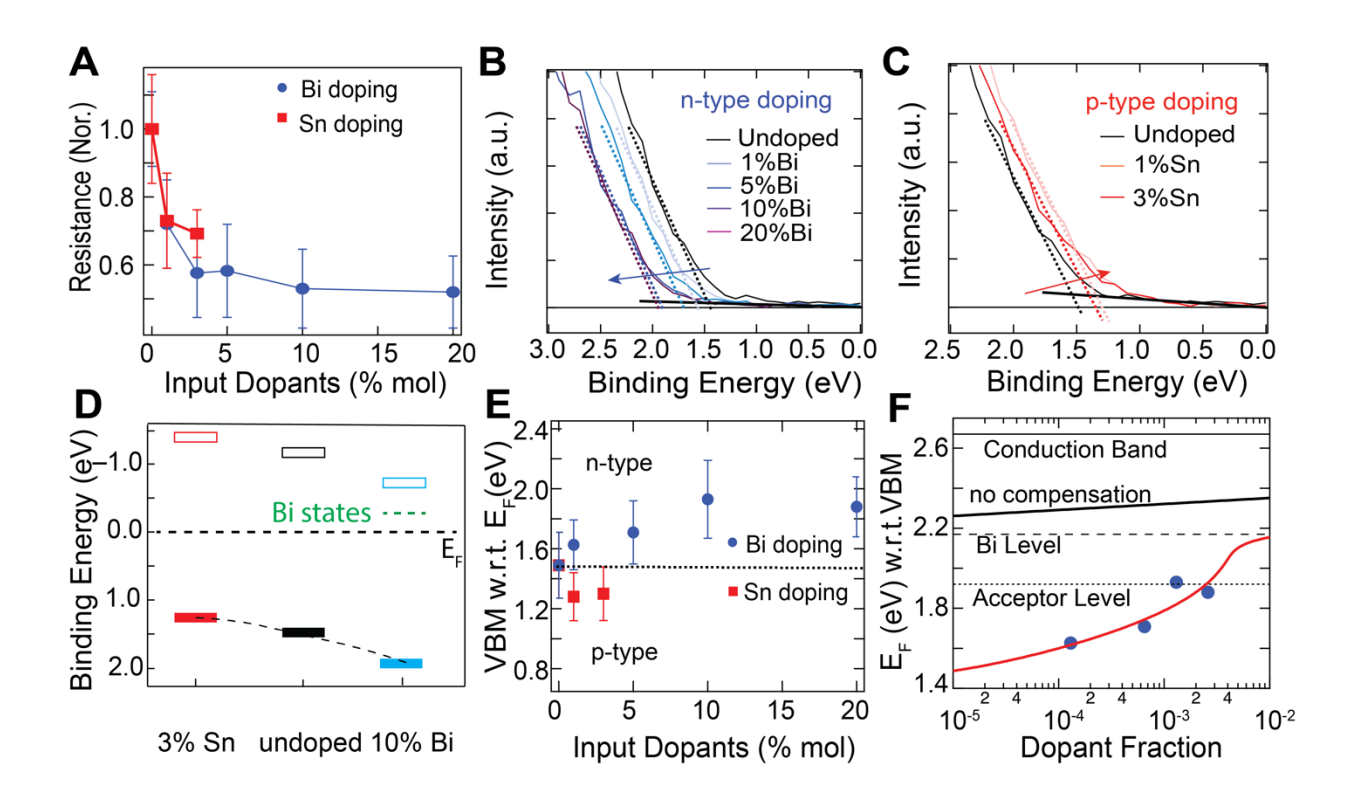


Figure 4. (A) Sheet resistance of PEA₂PbI₄ films versus dopant concentration. (B-C) HR-XPS spectra of the valence band edge region as a function of dopant concentration for Bi and Sn, respectively. (D) E_{VBM} with respect to E_F ($E_F - E_{VBM}$) as a function of dopant concentration, the CBM is plotted as unfilled rectangles and is determined as the VBM plus the electronic bandgap, taken here to be 2.67 eV. (E) Extracted band edge energies of undoped, Sn-, and Bi-doped PEA₂PbI₄ films with respect to Fermi level (set to zero here). To extract the E_{VBM} with respect to E_F ($E_F - E_{VBM}$), a linear fit of the photoelectron intensity onset is performed and the intersection with the baseline is extracted. (F) Fermi level with respect to the VBM (VBM is set to zero here) as a function of incorporated Bi dopant fraction. Blue dots: experimental data extracted from XPS results. Red line: model including a compensating trap level (Sec. XI in the SI). Black solid line: model without compensation.

Electronic doping mechanism in PEA₂PbI₄. Our data demonstrate that we can achieve both nand p-type electronic impurity doping through incorporating Bi and Sn, respectively. Figure 4E plots the extracted VBM (filled rectangles) as function of input dopant concentration, where the CBM (unfilled rectangles) are calculated by adding the electronic bandgap to the XPS determined VBM. However, in neither case is the conductivity increase or shift in Fermi level large. As noted above, the question of the mechanism of *p*-type doping through isovalent Sn_{Pb} substitution is complicated by the fact that isovalent substitution of Pb(II) by Sn(II) should not itself lead to p-doping since Sn(II) itself does not introduce acceptor levels according to chemical intuition and our extensive DFT simulations. The indirect doping through rendering the formation of V_{Pb} more favorable in close proximity to Sn_{Pb} can account for the p-type doping observed experimentally; in fact, it such a mechanism should be relatively inefficient (also in agreement with our experiments) due to the overall still low (but non-zero) probability of V_{Pb} formation. Alternatively, surface oxidation of Sn(II) species by residual oxidizing agents such as O₂ could be another

mechanism to account for the formation of holes in Sn(II) containing MHPs.¹⁷ In our experiments these processes are relatively inefficient as evinced by a Fermi level shift of only 220 meV. In contrast, while the dopant incorporation is much smaller with Bi doping, the Fermi level shift is two times larger, indicating a much higher doping efficiency for Bi compared to Sn, i.e. more delocalized carriers are introduced per dopant atom incorporation.

The n-type doping in 2D PEA₂PbI₄ by Bi³⁺ can be understood by direct substitutional doping (1). However, the shift in the Fermi level observed is smaller than what is expected for an impurity dopant, even with a deep-defect level of 0.5 eV below the conduction band. To illustrate, we plot the expected shift in Fermi level as a function of the fraction of dopant incorporation, $f_d = N_d/N_0$ (black solid line, Figure 4F), where N_d is the density of incorporated Bi defects and N_0 is the overall Pb density. A full derivation of the underlying physical model is provided in Sec. XI in the SI. There are two characteristic features where the measured data (blue circles in Figure 4F, extracted from Figure 4E by setting the VBM to zero) do not agree with the prediction; (1) the initial Fermi level shift is too small and (2) the subsequent shift in Fermi level position with increasing doping is larger than expected. In the case of normal doping the Fermi level position over the range of f_d values from 10^{-5} to 10^{-2} should vary from 2.25 eV to 2.35 eV (Figure 4F, black solid line) and would correspond to a doping efficiency $\eta = n_{el}/N_d$, where n_{el} is the dopant induced electron density, that is around 10⁻² and decreases with increasing dopant incorporation (Figure S11.4). However, our results suggest that the actual doping efficiency must be much lower (Figure 4F, blue circles), i.e., the measured Fermi level only varies from 1.5 eV to 1.9 eV with f_d varying between 10^{-4} to 10^{-2} . A model with a single dopant level, even if very deep (i.e., when E_d=1.5 eV) cannot explain these features, as shown in Figure S11.1. We therefore consider an alternative model that includes a fixed concentration of electron acceptors that are able to capture ionized electrons arising from the Bi dopant atoms.⁶⁷ Our model can reproduce the observed shifts in Fermi level position (red-trace, Figure 4F) when the fraction, $f_a =$ N_a/N_0 , where N_a is the density of electron acceptors, is $\sim 10^{-3}$ and the acceptor level is ~ 0.7 -0.8 eV below the CBM(dotted line in Figure 4F). Figures S11.2 and S11.3 further substantiate the specific acceptor level, ~ 0.7 -0.8 eV, and density, $\sim 10^{-3}$, showing that substantially different values can't reproduce our measured data similarly well. It is the consistency between the computationally derived defect level for Bi, the XPS-derived Fermi level shifts, and the observed changes in resistivity that lead us to consider the presence of this deeper acceptor population as the most likely current limit of our effort to electronically dope (PEA)₂PbI₄ with Bi. We also simulated the case where every incorporated Bi dopant produces a compensating defect, i.e., the concentration of compensating defects varies with input Bi dopant concentration, however, this could not reproduce our measurements. In fact, such a behavior would results in a completely pinned Fermi level (see Figure S11.5) which is clearly not observed here. Thus, we conclude that most of the Bi electrons are captured by a fixed concentration of acceptors, compensating the Bi dopant electrons.

There are several possible defects that could serve as the compensating acceptors. While in principle the unreduced Bi defect, i.e. reaction (2), would produce an empty state that could accept electrons at ~ 0.35 eV below the conduction band, we ruled this out because (1) in our simulations the acceptor states must be lower than ~0.7 eV to reproduce our data, (2) the calculated formation energy would suggest that the concentration of these defects would be too low to explain our data, and (3) we simulated the case where the acceptor level concentration varies with the impurity concentration and found this cannot explain the experimental observations (Figure S11.5). In 3D MAPbI₃ Nazeeruddin and co-workers⁶⁸ identified two point defects that accept electrons and are likely associated with iodine and MA. Similar point defects may also form in the 2D case and could be responsible for the observations reported here. Another potential source of an electron acceptor could be a tightly bound polaron. Li and co-workers found that small impurity dopants in 2D n=1 PEA₂PbI₄ can induce a self-trapped exciton that is ~ 0.7 eV below the band-edge.³¹ However, we can rule out a tightly bound polaron⁶⁹ as being responsible for the lower than expected doping efficiency since that would have the same statistics as a varying concentration of compensating defects which cannot reproduce our results or would lead to a lower effective defect level (i.e., lower than the computational value) but that also cannot explain our experimental results.

In future work, it would be valuable to subject the intrinsic and Bi-induced extrinsic defect landscape to a systematic computational search that resolves the detailed nature of the compensating defect revealed in our work. We stress, however, that such an investigation is not simple due to the enormous structural freedom afforded by the relatively open 2D PEA₂PbI₄ structure and large unit cell. Regarding Bi-doping, the success of the present work is to (1) experimentally quantify the extent of attainable n-type doping by Bi incorporation, (2) quantify the approximate depth of the Bi donor level by detailed and rather demanding high-level theory and (3) demonstrate that no single defect state can explain the observed degree of n-doping, revealing the existence of a compensating defect level.

Conclusion

We systematically studied the electronic doping of the prototype 2D perovskite PEA₂PbI₄ by using isovalent Sn^{2+} and aliovalent Bi^{3+} in both crystals and thin films. 4-point probe measurements and XPS data indicate that both Sn^{2+} and Bi^{3+} can moderately tune the carrier type and concentration, with Sn^{2+} as p-type dopant and Bi^{3+} as n-type dopant. We combined experimental observations with first-principles DFT simulations of defect-containing supercell models including up to 3,383 atoms to study impurity doping with high-level methods (spin-orbit coupled hybrid DFT). We found that both Sn and Bi dopants induce a slightly quenched exciton transition and a lower-energy absorption tail, and . DFT calculations confirm that Sn dopants decrease the bandgap of PEA₂PbI₄, while Bi dopants introduce defect states. Consistent with our calculations, Sn and Bi dopants do not appear to dramatically change the crystal structure of PEA₂PbI₄. We showed that substituting Pb²⁺ by Sn²⁺ is favorable, and the incorporation efficiency of Sn²⁺ is nearly 100%, indicating that the subsequent reaction to yield delocalized holes limits the electronic doping. We show that formation of V_{Pb} defects in close proximity to substituted Sn_{Pb} is one plausible doping mechanism

that would introduce more V_{Pb} vacancies and would lead to a shallow acceptor defect state. However, in the case of Bi^{3+} dopants, we observe two doping characteristics that differ from Sn^{2+} . First, Bi^{3+} incorporation is about 10 times smaller than that of 3D MAPbI₃ (incorporation efficiency of 0.18 in MAPbI₃, **Figure S9.1**⁷⁰). Second, the Bi doping efficiency, η (number of electrons introduced per incorporated dopant atom), while much higher than for Sn doping, is lower in the 2D compared to the 3D case. We hypothesize these issues could be associated with the more ionic and flexible lattice of 2D perovskites, which promotes the formation of various defects including metal vacancy, iodide vacancy, and interstitial iodide defects, making the aliovalent Bi^{3+} electronic doping less efficient. We found that for n-type doping the doping efficiency is limited by a population of acceptors. These compensating acceptors must be identified and avoided in order to fully un-pin the Fermi level in 2D perovskites

Methods

General methods. All sample preparations were performed using standard air-free techniques on a Schlenk line under nitrogen atmosphere or in a nitrogen-fill glovebox.

Materials. All chemicals were used as received unless otherwise indicated. Lead oxide (PbO, 99.999%), bismuth (III) oxide (Bi₂O₃, 99.999%), phenethylamine (PEA, \geq 99%), *N,N*-anhydrous DMF, 57% w/w aqueous hydriodic acid (HI) solution (99.95%, distilled, stabilized by H₃PO₂), and 50% w/w aqueous hypophosphorous acid solution were purchased from Sigma-Aldrich. Tin (IV) oxide (SnO₂, 99.9%) was purchased from Alfa-Aesar, and it was ground using a mortar and pestle before use.

Synthesis of (PEA)₂PbI₄ single crystals. 2D perovskite (PEA)₂PbI₄ single crystals were synthesized based on a previously reported cooling method.⁵ Briefly, 200 mg (0.90 mmol) of PbO and 200 μ L (1.59 mmol) of PEA were fully dissolved in 4 mL of HI and 0.5 mL of H₃PO₂ solution at 90 °C. The solution was then slowly cooled to room temperature at a rate of 2 °C/h, giving orange sheet-like crystals. The crystals were then isolated from the parent solution by vacuum filtration, washed by a small amount of diethyl ether, and dried under vacuum.

Synthesis of Bi-doped (PEA)₂PbI₄ single crystals. Bi-doped 2D perovskite (PEA)₂PbI₄ single crystals were synthesized by introducing a small amount of Bi₂O₃ to the reaction mixture. Briefly, PbO and Bi₂O₃ with different nominal ratios (Bi:Pb ratios of: 0.01, 0.03, 0.05, 0.1, and 0.2, with a total [PbO + Bi₂O₃] amount of 0.90 mmol) and 200 μ L (1.59 mmol) of PEA were fully dissolved at 90 °C in a solution containing 4 mL of HI solution and 0.5 mL of H₃PO₂. The solution is then slowly cooled to room temperature at a rate of 2 °C/h, giving dark-red to black sheet-like crystals. The crystals were then isolated from the parent solution by vacuum filtration, washed by a small amount of diethyl ether, and dried under vacuum.

Synthesis of Sn-doped (PEA)₂PbI₄ single crystals. Sn-doped 2D perovskite (PEA)₂PbI₄ single crystals were synthesized by introducing a small amount of SnO₂ to the reaction mixture. Generally, PbO and SnO₂ with different nominal ratios (Sn:Pb ratios of: 0.01, 0.03, 0.05, and 0.15, with a total [PbO + SnO₂] amount of 0.90 mmol) and 200 μ L (1.59 mmol) of PEA were fully dissolved at 90 °C in a solution containing 4 mL of HI solution and 0.5 mL of H₃PO₂. The solution was then slowly cooled to room temperature at a rate of 2 °C/h, giving red sheet-like crystals. The crystals were then isolated from the parent solution by vacuum filtration, washed by a small amount of diethyl ether, and dried under vacuum.

Preparation of undoped, Bi³⁺-doped, and Sn²⁺-doped (PEA)₂PbI₄ thin films. Quartz or FTO substrates were washed sequentially using acetone and isopropanol in a sonicator for 10 min each, followed by an

ultraviolet-ozone treatment for 15 min. Precursor solutions were prepared by dissolving corresponding crystals in DMF with 10 wt% (e.g. 20 mg in 200 μ L) and were immediately used. Thin films were prepared in a N₂-filled glovebox by spin coating the precursor solution onto substrates using a spin rate of 4000 rpm for 30 s, followed by thermal annealing at 100 °C for 10 min. Thin films on quartz substrates were used for UV-vis, PL, TRPL, and XRD measurements. Thin films on FTO were used for XPS, UPS, SEM, and EDX measurements.

Powder and single crystal X-ray diffraction. Powder X-ray diffraction measurements were collected on a Rigaku DMax 2200 diffractometer with a rotating Cu anode. Single-crystal diffraction data were collected on a Bruker D8 ADVANCE Series II instrument at 293 K using Mo K α radiation (λ = 0.71073 Å). A full sphere of diffraction data was collected and multi-scan empirical absorption correction was applied. Structure solution was obtained by direct methods using the SHELXS program and refined using the least-squares method by employing the SHELXL⁷¹ program within the Olex2 software⁷².

Optical absorption measurements. For powder absorption, powder samples were first obtained by grinding single crystals using mortar and pestle. Linear optical absorption spectra were obtained by performing optical diffuse reflectance measurements in a Cary 5000 UV-vis-NIR spectrometer operating in the 300 - 800 nm range at room temperature. A BaSO₄ pellet was used as the reference of 100% reflectance, and BaSO₄ powder was also used to dilute powder samples for all measurements. Linear optical absorption spectra of powders were generated by converting reflectance to absorption data using the Kubelka-Munk equation⁷³: $\alpha/S = (1 - R)^2/(2R)$, where R is the reflectance and α and S are the absorption and scattering coefficients, respectively. For thin film absorption, absorption spectra were collected in the transmission mode using a quartz substrate as the reference of 100% transmittance.

SEM and EDX measurements. SEM and EDS images were collected on a Hitachi 4800 SEM platform. SEM mapping was done at an electron beam condition of 3 kV and 2 μ A, while EDS mapping was done at an electron beam condition of 20 kV and 5 μ A for higher signal intensity.

XPS measurements. XPS measurements were acquired on a Physical Electronics Phi 5600 instrument. XPS high-resolution spectra were acquired using monochromatic Al-k α x-rays (h ν = 1486.7 eV), with a pass energy of 23.5 eV.

Four-point probe measurements. Four-point probe measurements were performed by using a Signatone four-point resistance system with a self-developed LabVIEW program. All measurements were conducted on thin films (on glass substrates) in dark conditions inside the nitrogen-filled glovebox. A Keithley source and meter were employed to source voltage and measure current. For each sample, current/voltage curves were measured and recorded, for at least five different positions on each sample, and sheet resistance was calculated and averages from the slope of the I/V curves.

First-principles calculations. The FHI-aims all-electron electronic structure software package was used to perform first principles DFT calculations.³⁷⁻⁴¹ FHI-aims is capable of computing properties of large and complex systems, enabling the semilocal and spin-orbit coupled hybrid DFT calculations reported in this work. The hybrid DFT implementation of Ref.³⁹ was optimized in detail for this work. Besides loop level optimizations to improve single core performance, the memory consumption and communication overhead within a compute node was reduced significantly by introducing shared-memory features standardized in version 3 of the message passing interface (MPI) standard into the code. On the multi node scale, the MPI communication patterns and the load-balancing were improved significantly to allow for efficient calculations on current, massively parallel computing architectures. Specifically, the Intel Skylake processor-based supercomputers Stampede2 (Texas Advanced Computing Center at The University of Texas at Austin through the XSEDE infrastructure) and Eagle at National Renewable Energy Laboratory were used for this work, employing several thousand CPU cores simultaneously for the largest computations reported in this work. We furthermore used the Max-Planck Computing and Data Facility's

Raven supercomputer. Exemplary timings are reported for one specific simulation (Figures 2E-H) in Table S12.1. Technical details of the overall improved hybrid DFT implementation in the FHI-aims code will be reported in a separate publication. Table S12.1 includes tabulated values for resources used in the (4x4)-Sn_{Pb} + V_{Pb} calculations. The Perdew-Berke-Ernzerhof (PBE)⁵⁴ density functional plus the Tkatchenko-Scheffler (TS) correction⁵⁵ for van der Waals (vdW) interactions was used to optimize the atomic coordinates and lattice parameters of each investigated structure model to reflect minima of the Born-Oppenheimer potential energy surface. "Tight" FHI-aims numerical default settings were used for relaxations. Past work on hybrid organic-inorganic perovskites has shown that this overall approach yields computational structure predictions in close agreement with experimental structures for organic-inorganic hybrid metal-halide semiconductors.^{6, 44, 50-51} The Heyd-Scuseria-Ernzerhof (HSE06) hybrid density functional⁷⁴⁻⁷⁵ with a screening parameter of 0.11 (Bohr radii)⁻¹, an exchange mixing parameter of 0.25, and non-self-consistent spin-orbit coupling (SOC)⁴¹ was used for calculations of band structure properties and orbital visualizations. 41, 74-75 See Figure S2.15 for the impact of SOC on electronic structure results for the doped system. "Intermediate" FHI-aims default settings were used for band structure and orbital calculations. A Gaussian broadening function of narrow width w was used to determine orbital occupations close to the boundary between unoccupied states (the FHI-aims defaults are w=0.01 eV for systems with an appreciable gap or w=0.05 eV for systems with a gap smaller than 0.2 eV between occupied and unoccupied states in the calculation). Gamma-centered $(n_1 \times n_2 \times n_3)$ k-point grids were chosen to be sufficiently dense by ensuring the products of n_i and lattice vector length |a_i| were at least 40 Å in length, where $|a_i|$ is the length of the ith real-space unit vector (i=1,2,3) and n_i is an integer in reciprocal space. A (2×2×2)k-point grid was used to relax the (4x4)-Snpb, (4x4)-Bipb, and (4x4)-Bi2vac structures. A (3×3×3) k-point grid was used to calculate the electronic structures of the (4x4) models. Additional k-point grids for the relaxations and electronic structure calculations of the smaller impurity models are included in the SI.

Associated Content

Supporting Information: Geometries, band structures and densities of states used in electronic structure simulations; XRD data and crystal structure refinement of Bi-doped PEA₂PbI₄; photophysical characterization, XPS, SEM and EDX data of Bi- and Sn-doped PEA₂PbI₄ thin films; comparison of Bi³⁺ doping efficiency for 3D MAPbI₃ and 2D PEA₂PbI₄; reaction equations and total energies used to compute defect formation energies; model of Fermi level position as a functon of dopant incorporation without and with consideration of compensating defects.

Notes

The authors declare no competing financial interest.

Acknowledgements

This work was primarily supported as part of the Center for Hybrid Organic Inorganic Semiconductors for Energy (CHOISE) an Energy Frontier Research Center funded by the Office of Basic Energy Sciences, Office of Science within the U.S. Department of Energy. Part of this work was authored by the Alliance for Sustainable Energy, LLC, the manager and operator of the National Renewable Energy Laboratory for DOE under contract no. DE-AC36-08GO28308. The views expressed in the article do not necessarily represent the views of the DOE or the U.S. Government. G.K. was supported by the National Science Foundation under awards number 1709294 and 1729297. Y.Y. acknowledges funding support through National Science Foundation under award number 1450280. D.B.M. acknowledges funding support through National Science Foundation under award number 2004869. This work used the Extreme Science and Engineering Discovery Environment (XSEDE), which is supported by National Science Foundation grant number ACI-1548562. Specifically, the work used the Stampede2 computer at Texas Advanced Computing Center through Allocation TG-DMR200077. Computer simulations were also carried out using resources of the

National Energy Research Scientific Computing Center (NERSC), a U.S. Department of Energy (DOE) Office of Science User Facility operated under Contract No. DE- AC02-05CH11231. A portion of the research was performed using computational resources sponsored by the Department of Energy's Office of Energy Efficiency and Renewable Energy and located at the National Renewable Energy Laboratory.

Data Availability

The data that supports findings in this paper can be found in the Supplementary Information. The very large geometry files for the 1,500-atom calculations were not included in SI due to their size. These files, and all other FHI-aims input and output files, can be found in the NOMAD repository, with individual digital object identifier URLs provided in the SI for each atomic structure model considered in this paper. Any additional data can be obtained through correspondence with the authors upon reasonable request.

References

- 1. Zhang, F.; Lu, H.; Tong, J.; Berry, J. J.; Beard, M. C.; Zhu, K., Advances in two-dimensional organic–inorganic hybrid perovskites. *Energy & Environmental Science* **2020**, *13* (4), 1154-1186.
- 2. Mao, L.; Stoumpos, C. C.; Kanatzidis, M. G., Two-Dimensional Hybrid Halide Perovskites: Principles and Promises. *Journal of the American Chemical Society* **2019**, *141* (3), 1171-1190.
- 3. Smith, I. C.; Hoke, E. T.; Solis-Ibarra, D.; McGehee, M. D.; Karunadasa, H. I., A Layered Hybrid Perovskite Solar-Cell Absorber with Enhanced Moisture Stability. *Angewandte Chemie International Edition* **2014**, *53* (42), 11232-11235.
- 4. Pedesseau, L.; Sapori, D.; Traore, B.; Robles, R.; Fang, H.-H.; Loi, M. A.; Tsai, H.; Nie, W.; Blancon, J.-C.; Neukirch, A.; Tretiak, S.; Mohite, A. D.; Katan, C.; Even, J.; Kepenekian, M., Advances and Promises of Layered Halide Hybrid Perovskite Semiconductors. *ACS Nano* **2016**, *10* (11), 9776-9786.
- 5. Lu, H.; Wang, J.; Xiao, C.; Pan, X.; Chen, X.; Brunecky, R.; Berry, J. J.; Zhu, K.; Beard, M. C.; Vardeny, Z. V., Spin-dependent charge transport through 2D chiral hybrid lead-iodide perovskites. *Science Advances* **2019**, *5* (12), eaay0571.
- 6. Jana, M. K.; Song, R.; Liu, H.; Khanal, D. R.; Janke, S. M.; Zhao, R.; Liu, C.; Valy Vardeny, Z.; Blum, V.; Mitzi, D. B., Organic-to-inorganic structural chirality transfer in a 2D hybrid perovskite and impact on Rashba-Dresselhaus spin-orbit coupling. *Nat Commun* **2020**, *11* (1), 4699.
- 7. Amerling, E.; Lu, H.; Larson, B. W.; Maughan, A. E.; Phillips, A.; Lafalce, E.; Whittaker-Brooks, L.; Berry, J. J.; Beard, M. C.; Vardeny, Z. V.; Blackburn, J. L., A Multi-Dimensional Perspective on Electronic Doping in Metal Halide Perovskites. *ACS Energy Letters* **2021**, *6* (3), 1104-1123.
- 8. Euvrard, J.; Yan, Y.; Mitzi, D. B., Electrical doping in halide perovskites. *Nature Reviews Materials* **2021**.
- 9. Salzmann, I.; Heimel, G.; Oehzelt, M.; Winkler, S.; Koch, N., Molecular Electrical Doping of Organic Semiconductors: Fundamental Mechanisms and Emerging Dopant Design Rules. *Accounts of Chemical Research* **2016**, *49* (3), 370-378.
- 10. Zhou, Y.; Chen, J.; Bakr, O. M.; Sun, H.-T., Metal-Doped Lead Halide Perovskites: Synthesis, Properties, and Optoelectronic Applications. *Chemistry of Materials* **2018**, *30* (19), 6589-6613.
- 11. Phung, N.; Félix, R.; Meggiolaro, D.; Al-Ashouri, A.; Sousa e Silva, G.; Hartmann, C.; Hidalgo, J.; Köbler, H.; Mosconi, E.; Lai, B.; Gunder, R.; Li, M.; Wang, K.-L.; Wang, Z.-K.; Nie, K.; Handick, E.; Wilks, R. G.; Marquez, J. A.; Rech, B.; Unold, T.; Correa-Baena, J.-P.; Albrecht, S.; De Angelis, F.; Bär, M.; Abate, A., The Doping Mechanism of Halide Perovskite Unveiled by Alkaline Earth Metals. *Journal of the American Chemical Society* **2020**, *142* (5), 2364-2374.

- 12. Abdelhady, A. L.; Saidaminov, M. I.; Murali, B.; Adinolfi, V.; Voznyy, O.; Katsiev, K.; Alarousu, E.; Comin, R.; Dursun, I.; Sinatra, L.; Sargent, E. H.; Mohammed, O. F.; Bakr, O. M., Heterovalent Dopant Incorporation for Bandgap and Type Engineering of Perovskite Crystals. *The Journal of Physical Chemistry Letters* **2016**, *7* (2), 295-301.
- 13. Liu, M.; Zhong, G.; Yin, Y.; Miao, J.; Li, K.; Wang, C.; Xu, X.; Shen, C.; Meng, H., Aluminum-Doped Cesium Lead Bromide Perovskite Nanocrystals with Stable Blue Photoluminescence Used for Display Backlight. *Advanced Science* **2017**, *4* (11), 1700335.
- 14. Pan, G.; Bai, X.; Yang, D.; Chen, X.; Jing, P.; Qu, S.; Zhang, L.; Zhou, D.; Zhu, J.; Xu, W.; Dong, B.; Song, H., Doping Lanthanide into Perovskite Nanocrystals: Highly Improved and Expanded Optical Properties. *Nano Lett.* **2017**, *17* (12), 8005-8011.
- 15. Zhou, D.; Liu, D.; Pan, G.; Chen, X.; Li, D.; Xu, W.; Bai, X.; Song, H., Cerium and Ytterbium Codoped Halide Perovskite Quantum Dots: A Novel and Efficient Downconverter for Improving the Performance of Silicon Solar Cells. *Advanced Materials* **2017**, *29* (42), 1704149.
- 16. Li, C.; Chen, X.; Li, N.; Liu, J.; Yuan, B.; Li, Y.; Wang, M.; Xu, F.; Wu, Y.; Cao, B., Highly conductive n-type CH3NH3Pbl3 single crystals doped with bismuth donors. *Journal of Materials Chemistry C* **2020**, *8* (11), 3694-3704.
- 17. Ricciarelli, D.; Meggiolaro, D.; Ambrosio, F.; De Angelis, F., Instability of Tin Iodide Perovskites: Bulk p-Doping versus Surface Tin Oxidation. *ACS Energy Letters* **2020,** *5* (9), 2787-2795.
- 18. Meggiolaro, D.; Ricciarelli, D.; Alasmari, A. A.; Alasmary, F. A. S.; De Angelis, F., Tin versus Lead Redox Chemistry Modulates Charge Trapping and Self-Doping in Tin/Lead Iodide Perovskites. *The Journal of Physical Chemistry Letters* **2020**, *11* (9), 3546-3556.
- 19. Lyons, J. L., Effective Donor Dopants for Lead Halide Perovskites. *Chemistry of Materials* **2021**, *33* (15), 6200-6205.
- 20. Kang, Y.; Kang, S.; Han, S., Influence of Bi doping on physical properties of lead halide perovskites: a comparative first-principles study between CsPbI3 and CsPbBr3. *Materials Today Advances* **2019**, *3*, 100019.
- 21. Yu, Z.-L.; Zhao, Y.-Q.; Wan, Q.; Liu, B.; Yang, J.-L.; Cai, M.-Q., Theoretical study on the effect of the optical properties and electronic structure for the Bi-doped CsPbBr3. *Journal of Physics: Condensed Matter* **2020**, *32* (20), 205504.
- 22. Yin, J.; Ahmed, G. H.; Bakr, O. M.; Brédas, J.-L.; Mohammed, O. F., Unlocking the Effect of Trivalent Metal Doping in All-Inorganic CsPbBr3 Perovskite. *ACS Energy Letters* **2019**, *4* (3), 789-795.
- 23. Mosconi, E.; Merabet, B.; Meggiolaro, D.; Zaoui, A.; De Angelis, F., First-Principles Modeling of Bismuth Doping in the MAPbl3 Perovskite. *The Journal of Physical Chemistry C* **2018**, *122* (25), 14107-14112.
- 24. Zhang, X.; Shen, J.-X.; Turiansky, M. E.; Van de Walle, C. G., Hidden role of Bi incorporation in nonradiative recombination in methylammonium lead iodide. *Journal of Materials Chemistry A* **2020**, *8* (26), 12964-12967.
- 25. Pizzochero, M.; Barin, G. B.; Čerņevičs, K. n.; Wang, S.; Ruffieux, P.; Fasel, R.; Yazyev, O. V., Edge Disorder in Bottom-Up Zigzag Graphene Nanoribbons: Implications for Magnetism and Quantum Electronic Transport. *The Journal of Physical Chemistry Letters* **2021**, *12* (19), 4692-4696.
- 26. Lyu, F.; Zheng, X.; Wang, Y.; Shi, R.; Yang, J.; Li, Z.; Yu, J.; Lin, B.-L., Bi3+ doped 2D Ruddlesden–Popper organic lead halide perovskites. *Journal of Materials Chemistry A* **2019**, *7* (26), 15627-15632.
- 27. Cortecchia, D.; Mróz, W.; Neutzner, S.; Borzda, T.; Folpini, G.; Brescia, R.; Petrozza, A., Defect Engineering in 2D Perovskite by Mn(II) Doping for Light-Emitting Applications. *Chem* **2019**, *5* (8), 2146-2158.
- 28. Zhang, L.; Jiang, T.; Yi, C.; Wu, J.; Liu, X.-K.; He, Y.; Miao, Y.; Zhang, Y.; Zhang, H.; Xie, X.; Wang, P.; Li, R.; Gao, F.; Huang, W.; Wang, J., Bright Free Exciton Electroluminescence from Mn-Doped Two-Dimensional Layered Perovskites. *The Journal of Physical Chemistry Letters* **2019**, *10* (11), 3171-3175.

- 29. Ba, Q.; Jana, A.; Wang, L.; Kim, K. S., Dual Emission of Water-Stable 2D Organic–Inorganic Halide Perovskites with Mn(II) Dopant. *Advanced Functional Materials* **2019**, *29* (43), 1904768.
- 30. Biswas, A.; Bakthavatsalam, R.; Kundu, J., Efficient Exciton to Dopant Energy Transfer in Mn2+-Doped (C4H9NH3)2PbBr4 Two-Dimensional (2D) Layered Perovskites. *Chemistry of Materials* **2017**, *29* (18), 7816-7825.
- 31. Li, T.; Chen, X.; Wang, X.; Lu, H.; Yan, Y.; Beard, M. C.; Mitzi, D. B., Origin of Broad-Band Emission and Impact of Structural Dimensionality in Tin-Alloyed Ruddlesden–Popper Hybrid Lead Iodide Perovskites. *ACS Energy Letters* **2020**, *5* (2), 347-352.
- 32. Passarelli, J. V.; Mauck, C. M.; Winslow, S. W.; Perkinson, C. F.; Bard, J. C.; Sai, H.; Williams, K. W.; Narayanan, A.; Fairfield, D. J.; Hendricks, M. P.; Tisdale, W. A.; Stupp, S. I., Tunable exciton binding energy in 2D hybrid layered perovskites through donor—acceptor interactions within the organic layer. *Nature Chemistry* **2020**, *12* (8), 672-682.
- 33. Jiang, Q.; Ni, Z.; Xu, G.; Lin, Y.; Rudd, P. N.; Xue, R.; Li, Y.; Li, Y.; Gao, Y.; Huang, J., Interfacial Molecular Doping of Metal Halide Perovskites for Highly Efficient Solar Cells. *Advanced Materials* **2020**, *32* (31), 2001581.
- 34. Euvrard, J.; Gunawan, O.; Zhong, X.; Harvey, S. P.; Kahn, A.; Mitzi, D. B., p-Type molecular doping by charge transfer in halide perovskite. *Materials Advances* **2021**, *2* (9), 2956-2965.
- 35. Calabrese, J.; Jones, N. L.; Harlow, R. L.; Herron, N.; Thorn, D. L.; Wang, Y., Preparation and characterization of layered lead halide compounds. *J Am Chem Soc* **1991**, *113* (6), 2328-2330.
- 36. Perdew, J. P.; Yang, W.; Burke, K.; Yang, Z.; Gross, E. K. U.; Scheffler, M.; Scuseria, G. E.; Henderson, T. M.; Zhang, I. Y.; Ruzsinszky, A.; Peng, H.; Sun, J.; Trushin, E.; Görling, A., Understanding band gaps of solids in generalized Kohn–Sham theory. *Proceedings of the National Academy of Sciences* **2017**, *114* (11), 2801-2806.
- 37. Blum, V.; Gehrke, R.; Hanke, F.; Havu, P.; Havu, V.; Ren, X.; Reuter, K.; Scheffler, M., Ab initio molecular simulations with numeric atom-centered orbitals. *Computer Physics Communications* **2009**, *180* (11), 2175-2196.
- 38. Havu, V.; Blum, V.; Havu, P.; Scheffler, M., Efficient O(N) integration for all-electron electronic structure calculation using numeric basis functions. *Journal of Computational Physics* **2009**, *228* (22), 8367-8379.
- 39. Levchenko, S. V.; Ren, X.; Wieferink, J.; Johanni, R.; Rinke, P.; Blum, V.; Scheffler, M., Hybrid functionals for large periodic systems in an all-electron, numeric atom-centered basis framework. *Computer Physics Communications* **2015**, *192*, 60-69.
- 40. Knuth, F.; Carbogno, C.; Atalla, V.; Blum, V.; Scheffler, M., All-electron formalism for total energy strain derivatives and stress tensor components for numeric atom-centered orbitals. *Computer Physics Communications* **2015**, *190*, 33-50.
- 41. Huhn, W. P.; Blum, V., One-hundred-three compound band-structure benchmark of post-self-consistent spin-orbit coupling treatments in density functional theory. *Physical Review Materials* **2017**, *1* (3), 033803.
- 42. Gómez-Abal, R.; Li, X.; Scheffler, M.; Ambrosch-Draxl, C., Influence of the Core-Valence Interaction and of the Pseudopotential Approximation on the Electron Self-Energy in Semiconductors. *Physical Review Letters* **2008**, *101* (10), 106404.
- 43. Chen, X.; Lu, H.; Li, Z.; Zhai, Y.; Ndione, P. F.; Berry, J. J.; Zhu, K.; Yang, Y.; Beard, M. C., Impact of Layer Thickness on the Charge Carrier and Spin Coherence Lifetime in Two-Dimensional Layered Perovskite Single Crystals. *ACS Energy Letters* **2018**, *3* (9), 2273-2279.
- 44. Lu, H.; Xiao, C.; Song, R.; Li, T.; Maughan, A. E.; Levin, A.; Brunecky, R.; Berry, J. J.; Mitzi, D. B.; Blum, V.; Beard, M. C., Highly Distorted Chiral Two-Dimensional Tin Iodide Perovskites for Spin Polarized Charge Transport. *Journal of the American Chemical Society* **2020**, *142* (30), 13030-13040.

- 45. Eperon, G. E.; Ginger, D. S., B-Site Metal Cation Exchange in Halide Perovskites. *ACS Energy Letters* **2017**, *2* (5), 1190-1196.
- 46. Kroupa, D. M.; Hughes, B. K.; Miller, E. M.; Moore, D. T.; Anderson, N. C.; Chernomordik, B. D.; Nozik, A. J.; Beard, M. C., Synthesis and Spectroscopy of Silver-Doped PbSe Quantum Dots. *J Am Chem Soc* **2017**, *139* (30), 10382-10394.
- 47. Lu, H.; Carroll, G. M.; Chen, X.; Amarasinghe, D. K.; Neale, N. R.; Miller, E. M.; Sercel, P. C.; Rabuffetti, F. A.; Efros, A. L.; Beard, M. C., n-Type PbSe Quantum Dots via Post-Synthetic Indium Doping. *J Am Chem Soc* **2018**, *140* (42), 13753-13763.
- 48. Blackburn, J. L.; Ferguson, A. J.; Reid, O. G., Spectroscopy of Ground- and Excited-State Charge Carriers in Single-Wall Carbon Nanotubes. In *Handbook of Carbon Nanomaterials*, World Scientific: 2017; Vol. Volume 9 & 10, pp 237-296.
- 49. Krukau, A. V.; Vydrov, O. A.; Izmaylov, A. F.; Scuseria, G. E., Influence of the exchange screening parameter on the performance of screened hybrid functionals. *The Journal of Chemical Physics* **2006**, *125* (22), 224106.
- 50. Jana, M. K.; Janke, S. M.; Dirkes, D. J.; Dovletgeldi, S.; Liu, C.; Qin, X.; Gundogdu, K.; You, W.; Blum, V.; Mitzi, D. B., Direct-Bandgap 2D Silver—Bismuth Iodide Double Perovskite: The Structure-Directing Influence of an Oligothiophene Spacer Cation. *Journal of the American Chemical Society* **2019**, *141* (19), 7955-7964.
- 51. Liu, C.; Huhn, W.; Du, K.-Z.; Vazquez-Mayagoitia, A.; Dirkes, D.; You, W.; Kanai, Y.; Mitzi, D. B.; Blum, V., Tunable Semiconductors: Control over Carrier States and Excitations in Layered Hybrid Organic-Inorganic Perovskites. *Physical Review Letters* **2018**, *121* (14), 146401.
- 52. Steger, M.; Janke, S. M.; Sercel, P. C.; Larson, B. W.; Lu, H.; Qin, X.; Yu, V. W.-z.; Blum, V.; Blackburn, J. L., On the optical anisotropy in 2D metal-halide perovskites. *Nanoscale* **2022**.
- 53. Kim, S.; Lee, M.; Hong, C.; Yoon, Y.; An, H.; Lee, D.; Jeong, W.; Yoo, D.; Kang, Y.; Youn, Y.; Han, S., A band-gap database for semiconducting inorganic materials calculated with hybrid functional. *Scientific Data* **2020**, *7* (1), 387.
- 54. Perdew, J. P.; Burke, K.; Ernzerhof, M., Generalized Gradient Approximation Made Simple. *Phys. Rev. Lett.* **1996**, *77* (18), 3865-3868.
- 55. Tkatchenko, A.; Scheffler, M., Accurate Molecular Van Der Waals Interactions from Ground-State Electron Density and Free-Atom Reference Data. *Physical Review Letters* **2009**, *102* (7), 073005.
- 56. Deák, P.; Aradi, B.; Frauenheim, T.; Janzén, E.; Gali, A., Accurate defect levels obtained from the HSE06 range-separated hybrid functional. *Physical Review B* **2010**, *81* (15), 153203.
- 57. Chagas da Silva, M.; Lorke, M.; Aradi, B.; Farzalipour Tabriz, M.; Frauenheim, T.; Rubio, A.; Rocca, D.; Deák, P., Self-Consistent Potential Correction for Charged Periodic Systems. *Physical Review Letters* **2021**, *126* (7), 076401.
- 58. Freysoldt, C.; Grabowski, B.; Hickel, T.; Neugebauer, J.; Kresse, G.; Janotti, A.; Van de Walle, C. G., First-principles calculations for point defects in solids. *Reviews of Modern Physics* **2014**, *86* (1), 253-305.
- 59. Gake, T.; Kumagai, Y.; Freysoldt, C.; Oba, F., Finite-size corrections for defect-involving vertical transitions in supercell calculations. *Physical Review B* **2020**, *101* (2), 020102.
- 60. Kim, Y.-S.; Marsman, M.; Kresse, G.; Tran, F.; Blaha, P., Towards efficient band structure and effective mass calculations for III-V direct band-gap semiconductors. *Physical Review B* **2010**, *82* (20), 205212.
- 61. Goyal, A.; McKechnie, S.; Pashov, D.; Tumas, W.; van Schilfgaarde, M.; Stevanović, V., Origin of Pronounced Nonlinear Band Gap Behavior in Lead–Tin Hybrid Perovskite Alloys. *Chemistry of Materials* **2018**, *30* (11), 3920-3928.
- 62. Mao, L.; Tsai, H.; Nie, W.; Ma, L.; Im, J.; Stoumpos, C. C.; Malliakas, C. D.; Hao, F.; Wasielewski, M. R.; Mohite, A. D.; Kanatzidis, M. G., Role of Organic Counterion in Lead- and Tin-Based Two-

- Dimensional Semiconducting Iodide Perovskites and Application in Planar Solar Cells. *Chemistry of Materials* **2016**, *28* (21), 7781-7792.
- 63. Li, J.; Yu, Q.; He, Y.; Stoumpos, C. C.; Niu, G.; Trimarchi, G. G.; Guo, H.; Dong, G.; Wang, D.; Wang, L.; Kanatzidis, M. G., Cs2Pbl2Cl2, All-Inorganic Two-Dimensional Ruddlesden—Popper Mixed Halide Perovskite with Optoelectronic Response. *Journal of the American Chemical Society* **2018**, *140* (35), 11085-11090.
- 64. Zhao, Y.-Q.; Ma, Q.-R.; Liu, B.; Yu, Z.-L.; Yang, J.; Cai, M.-Q., Layer-dependent transport and optoelectronic property in two-dimensional perovskite: (PEA)2PbI4. *Nanoscale* **2018**, *10* (18), 8677-8688.
- 65. Konstantakou, M.; Stergiopoulos, T., A critical review on tin halide perovskite solar cells. *Journal of Materials Chemistry A* **2017**, *5* (23), 11518-11549.
- Dalpian, G. M.; Liu, Q.; Stoumpos, C. C.; Douvalis, A. P.; Balasubramanian, M.; Kanatzidis, M. G.; Zunger, A., Changes in charge density vs changes in formal oxidation states: The case of Sn halide perovskites and their ordered vacancy analogues. *Physical Review Materials* **2017**, *1* (2), 025401.
- 67. Tietze, M. L.; Pahner, P.; Schmidt, K.; Leo, K.; Lüssem, B., Doped Organic Semiconductors: Trap-Filling, Impurity Saturation, and Reserve Regimes. *Advanced Functional Materials* **2015**, *25* (18), 2701-2707.
- 68. Heo, S.; Seo, G.; Lee, Y.; Lee, D.; Seol, M.; Lee, J.; Park, J.-B.; Kim, K.; Yun, D.-J.; Kim, Y. S.; Shin, J. K.; Ahn, T. K.; Nazeeruddin, M. K., Deep level trapped defect analysis in CH3NH3Pbl3 perovskite solar cells by deep level transient spectroscopy. *Energy & Environmental Science* **2017**, *10* (5), 1128-1133.
- 69. Srimath Kandada, A. R.; Silva, C., Exciton Polarons in Two-Dimensional Hybrid Metal-Halide Perovskites. *The Journal of Physical Chemistry Letters* **2020**, *11* (9), 3173-3184.
- 70. Wang, R.; Zhang, X.; He, J.; Ma, C.; Xu, L.; Sheng, P.; Huang, F., Bi3+-doped CH3NH3Pbl3: Redshifting absorption edge and longer charge carrier lifetime. *Journal of Alloys and Compounds* **2017**, *695*, 555-560.
- 71. Sheldrick, G., Crystal structure refinement with SHELXL. *Acta Crystallographica Section C* **2015**, 71 (1), 3-8.
- 72. Dolomanov, O. V.; Bourhis, L. J.; Gildea, R. J.; Howard, J. A. K.; Puschmann, H., OLEX2: a complete structure solution, refinement and analysis program. *Journal of Applied Crystallography* **2009**, *42* (2), 339-341.
- 73. Kortüm, G.; Braun, W.; Herzog, G., Principles and Techniques of Diffuse-Reflectance Spectroscopy. *Angewandte Chemie International Edition in English* **1963,** *2* (7), 333-341.
- 74. Heyd, J.; Scuseria, G. E.; Ernzerhof, M., Hybrid functionals based on a screened Coulomb potential. *The Journal of Chemical Physics* **2003**, *118* (18), 8207-8215.
- 75. Heyd, J.; Scuseria, G. E.; Ernzerhof, M., Erratum: "Hybrid functionals based on a screened Coulomb potential" [J. Chem. Phys. 118, 8207 (2003)]. *The Journal of Chemical Physics* **2006**, *124* (21), 219906.